The Exoplanet Characterization Observatory (EChO): performance model *EclipseSim* and applications

Roy van Boekel[a] Björn Benneke[b] Kevin Heng[c] Renyu Hu[b] Nikku Madhusudhan[d] Sascha Quanz[c] Yan Bétrémieux[a] Jeroen Bouwman[a] Guo Chen[a] Leen Decin[e] Remco de Kok[f] Adrian Glauser[a] Manuel Güdel[g] Peter Hauschildt[h] Thomas Henning[a] Sandra Jeffers[i] Sheng Jin[a] Lisa Kaltenegger[a,j] Franz Kerschbaum[g] Oliver Krause[a] Helmut Lammer[k] Armin Luntzer[g] Michael Meyer[c] Yamila Miguel[a] Christoph Mordasini[a] Roland Ottensamer[g] Theresa Rank-Lueftinger[g] Ansgar Reiners[i] Timo Reinhold[i] Hans Martin Schmid[c] Ignas Snellen[l] Daphne Stam[f] Zhao Sun[a] Bart Vandenbussche[e]

[a] Max Planck-Institute for Astronomy, Königstuhl 17, D-69120 Heidelberg, Germany;
[b] Massachusetts Institute of Technology, Department of Earth, Atmospheric and Planetary Sciences, 77 Massachusetts Avenue, Cambridge, MA 02139, USA
[c] Institute for Astronomy, ETH Zürich, Wolfgang-Pauli-Strasse 27, 8093, Zürich, Switzerland;
[d] Department of Physics and Department of Astronomy, Yale University, 260 Whitney Avenue, New Haven, CT 06511, USA;
[e] Institute of Astronomy, Celestijnenlaan 200D, BUS 2401, 3001 Leuven, Belgium;
[f] SRON Netherlands Institute for Space Research, Sorbonnelaan 2, 3584 CA Utrecht, The Netherlands;
[g] University of Vienna, Dept. of Astrophysics,Türkenschanzstraße 17, 1180 Wien, Austria;
[h] Hamburger Sternwarte, Gojenbergsweg 112, 21029 Hamburg, Germany;
[i] Institut für Astrophysik Göttingen, Friedrich-Hund-Platz 1, D-37077 Göttingen, Germany;
[j] Harvard-Smithsonian Center for Astrophysics, 60 Garden St. MS20, Cambridge, MA 02138, USA;
[k] Institut für Weltraumforschung, Schmiedlstraße 6, 8042 Graz, Austria;
[l] Leiden Observatory, Leiden University, Postbus 9513, 2300 RA, Leiden, The Netherlands

ABSTRACT

We present *EclipseSim*, a radiometric model for exoplanet transit spectroscopy that allows easy exploration of the fundamental performance limits of any space-based facility aiming to perform such observations. It includes a library of stellar model atmosphere spectra and can either approximate exoplanet spectra by simplified models, or use any theoretical or observed spectrum, to simulate observations. All calculations are done in a spectrally resolved fashion and the contributions of the various fundamental noise sources are budgeted separately, allowing easy assessment of the dominant noise sources, as a function of wavelength. We apply *EclipseSim*to the Exoplanet Characterization Observatory (EChO), a proposed mission dedicated to exoplanet transit spectroscopy that is currently in competition for the M3 launch slot of ESA's cosmic vision programme. We show several case studies on planets with sizes in the super-Earth to Jupiter range, and temperatures ranging from the temperate to the $\approx$1500 K regime, demonstrating the power and versatility of EChO. *EclipseSim* is publicly available*.

Keywords: EChO, exoplanets, characterization, transit spectroscopy, radiometric model

Further author information: Send correspondence to RvB: E-mail: boekel@mpia.de
*If you are interested in using *EclipseSim*, please visit http://www.mpia-hd.mpg.de/homes/boekel/EclipseSim/

Space Telescopes and Instrumentation 2012: Optical, Infrared, and Millimeter Wave, edited by Mark C. Clampin, Giovanni G. Fazio, Howard A. MacEwen, Jacobus M. Oschmann, Jr., Proc. of SPIE Vol. 8442, 84421F

1. INTRODUCTION

Pioneering efforts to detect radiation emitted, absorbed, or scattered by exoplanetary atmospheres have opened the field of exoplanet atmosphere characterization (see e.g.[1] for a review). These first works have inspired a multitude of theoretical studies of the chemistry (e.g.[2]) and dynamics (e.g.[3,4]) associated with these atmospheres. The next frontier in the study of exoplanets is the procurement of high-quality transmission and emission spectra of a large sample of targets, via a dedicated space mission. The *E*xoplanet *Ch*aracterization *O*bservatory (ECho[5,6]) is a proposed mission aiming to do this that is currently in competition for the M3 launch slot in ESA's cosmic vision programme.

Spectroscopy is the method of choice for exoplanet characterization. The main spectroscopically active molecules (e.g. H_2O, CH_4, CO_2, CO, NH_3; e.g.[7,8]) can be identified due to their strong near-infrared ro-vibrational bands and their relative abundances can be accurately measured, allowing the (non-equilibrium) chemistry to be probed. This is intimately linked to the gas dynamics, transporting reaction products vertically and horizontally through the atmosphere on short timescales. At optical wavelengths, the scattering of radiation in the atmosphere may be detected (e.g.[9–11]), yielding measurements of also spectroscopically inactive species that often make up the bulk of the atmospheric mass (H_2, He, O_2, N_2; e.g.[12,13]). This allows one to estimate the absolute abundances of the various previously mentioned molecules, and thus to determine to what degree the atmospheres of planets have been enriched in heavy elements (or "metals"). Comparison of planet and host-star metallicity provides critical insights into the planet formation process, in particular on the accretion history in the primordial circumstellar disk (e.g.[14,15]). In addition, the abundances of these elements thought to be crucial for the emergence of life (C,H,O,N) might have implications on the potential for habitability in these systems. The combination of optical and near-infrared observations provides constraints on the presence of clouds (e.g.[16]), as well as high-altitude continuum absorbers that cause stratospheres in some planets but not in others (e.g.[17]). The combination of optical and infrared spectra furthermore constrains the energy balance of the planet, i.e. its "climate" (e.g.[18,19]).

In order to achieve these goals, EChO must provide spectra of sufficient quality to enable accurate estimates of temperature and pressure profiles in the atmospheres, as well as constraints on the contribution due to Rayleigh scattering in the atmosphere. In preparation for this mission we have developed the radiometric model *EclipseSim*. We adopt a simple but general approach that allows for an easy comparison of different telescope and instrument combinations, and can be used to identify the "sweet spots" of a specific facility. We calculate the fundamental limit on the SNR of exoplanet spectra that can be obtained, assuming that instrumental systematic effects can either be avoided by employing a facility design optimized for stability, or be removed in post-processing. That is, given a set of assumptions on telescope and instrument parameters, we calculate the photon noise limit achievable on spectra of exoplanets with a range of parameters, orbiting host stars with a range of parameters. An earlier radiometric model was applied to EchO[20] on which *EclipseSim* improves by performing fully spectrally resolved instead of mono-chromatic simulations (allowing to also create simulated data), including stellar photosphere models instead of blackbody approximations, and including the zodiacal background which is critical at wavelengths beyond $\approx 10\,\mu$m. Our model also accounts for the noise introduced by the pre- and post-eclipse "baseline" measurement, contrary to the earlier model[20] in which this was assumed to be negligible.

1.1 Exoplanet transit spectroscopy: the measurement principle

The primary challenge in any kind of exoplanet characterization effort is to overcome the huge brightness contrast between the planet and the host star. This may be done by spatially resolving the light from star and planet using high-contrast imaging or interferometric techniques, which works best for nearby, young systems with large orbital separations. An alternative approach can be used for transiting systems, whose average orbital radii are naturally biased to very small values. Here, we cannot directly separate the light from star and planet, but instead we try to detect the imprint of the planet atmosphere in the form of *minute temporal variations in the combined light*. The principle of the combined light method is illustrated in figure 1. We distinguish between three observational cases:

- in *primary eclipse* (often called "transit") the planet moves in front of the star, blocking a fraction of the starlight approximately equal to the ratio of solid angles subtended by planet and star[†]. At the planet limb the high atmospheric layers are partially transparent, and those atmospheric constituents that have spectral features in their opacity curves will cause minute wavelength-dependent variations in the observed eclipse depth, from which we can establish their presence and relative abundances.
- in *secondary eclipse* (often called "occultation") the planet moves behind the star. Before and after the eclipse we see the sum of star and planet light, during the eclipse we see only the star, and the difference yields the amount of light emitted from the planet day side, which in the infrared will typically be dominated by thermal emission and in the optical by reflected stellar light. This allows do detect spectroscopically active species, to constrain the (vertical) temperature structure of the planet atmosphere, and to measure the optical albedo.
- in *phase resolved observations* (also called "around the orbit monitoring") we measure the system flux over a much longer time than during eclipse observations, typically for at least half an orbit. This allows measuring flux contrasts over the planet surface in the longitudinal direction[‡] which, when the light curve includes a secondary ecilpse, can be converted into a lattitude-averaged flux (or "brightness temperature") map of the planetary surface. In principle, this method can also be used to observe non-transiting systems, in which case only the brightness variations over the surface can be measured, but not the brightness in absolute sense, since the latter information is encoded in the secondary eclipse depth.

In all three cases the signature of the planet atmosphere is encoded in minute, wavelength dependent variations of the system flux with time. Our direct, observational goal is thus to monitor the system flux with very high spectro-photometric sensitivity and stability. The typical time scale of eclise measurements is given by the eclipse duration and the need to have sufficient "baseline" before and after the eclipse, and is ≈2 to ≈10 hours. The time scale for phase resolved measurements will typically be ≈1 to a few days.

2. PLANET AND HOST STAR SPECTRA

2.1 Host star spectra

Exoplanet host stars that will be considered for transit observations will normally be main sequence stars. For these, we wish to predict the number of stellar photons in each wavelength bin for a system with a given distance or, conversely, for a given apparent brightness. Combinations of effective temperature, radius, and mass appropriate for main sequence stars are given by stellar evolutionary models. The emergent photospheric intensities are then obtained by interpolating a pre-calculated grid of PHOENIX stellar model atmosphere spectra at the corresponding effective temperatures and surface gravities, the absolute brightness being set by the stellar radius. The observed stellar spectrum is given by:

$$F_*(\lambda) = \frac{\pi R_*^2}{d^2} I(T_\mathrm{p}, \lambda) \tag{1}$$

where R_* denotes the stellar radius, d is the distance between the modeled star+planet system and the telescope, and $I(T_\mathrm{p}, \lambda)$ is the intensity of the stellar photosphere, averaged over the stellar disk as seen by a distant observer (i.e. including limb-darkening). See appendix A for a detailed description of the adopted stellar parameters.

[†]In detail, the shape and depth of a primary eclipse light curve depend on the exact eclipse path of the planet over the stellar surface, the stellar limb-darkening law, and any brightness variations on the stellar surface due to e.g. star spots.

[‡]These observations will typically be done for hot, short-period planets that are expected to be tidally locked, i.e. their orbital and rotational periods are equal. Hence, the day and night side. Thus, the physical planet longitude that is facing us is directly correlated with the orbital phase, and by measuring the brightness of the planet as a function of orbital phase, we also measure it as a function of longitude on the planet surface.

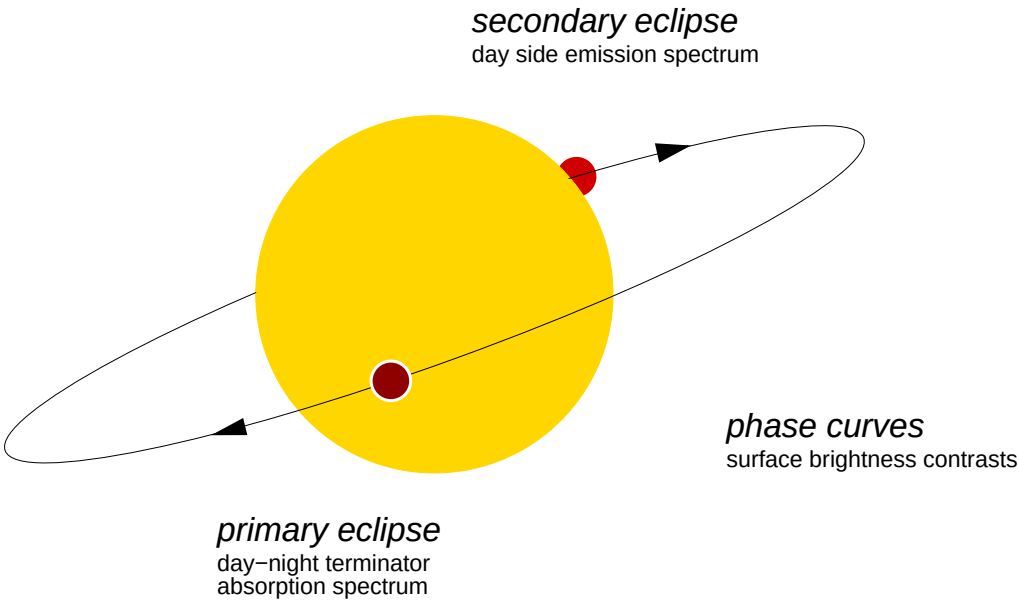

Figure 1. An illustration of the geometry employed in the transit method (after Seager & Deming[1]). A color version of this figure is available online.

2.2 Planet spectra

There are two ways to incorporate exoplanet emission or transmission spectra in the radiometric calculations: (1) read a spectrum from file. This can be an observed spectrum or the output of any planetary atmosphere code that calculates these quantities, from file; or (2) have the code calculate simple, approximative emission and transmission spectra. Option (1) is useful for studying specific aspects or systems in detail, for example in retrieval experiments. Option two is best used for statistical feasibility assessments. Here, we describe the calculations performed for the latter option.

2.2.1 Day-side emission spectra in secondary eclipse

In secondary eclipse we observe light coming from the planet's day side. At optical wavelengths this is typically dominated by stellar photons scattered by the planet atmosphere (or reflected off the surface), while in the infrared we see the planet's thermal emission.

Planet reflected light

The amount of light reflected by the planet depends on the wavelength-dependent albedo $A(\lambda)$, i.e. the fraction of incoming stellar radiation that is scattered away from the planet, as well as on the planet size and orbital radius, and is given by:

$$F_{\mathrm{p,r}}(\lambda) = F_*(\lambda) x_{\mathrm{r}}(\lambda) A(\lambda) \frac{R_{\mathrm{p}}^2}{a^2} \tag{2}$$

where $F_*(\lambda)$ is the observed stellar spectrum, $x_{\mathrm{r}}(\lambda)$ is a parameter controlling how efficiently stellar radiation is back-scattered towards the observer. The often used "geometric" albedo is then $A_{\mathrm{g}}(\lambda) = x_{\mathrm{r}}(\lambda)A(\lambda)$. By default we use $x_{\mathrm{r}}(\lambda) = 2/3$ (independent of wavelength), appropriate for an isotropically scattering, i.e. "Lambertian", spherical body. Note that equation 2 does not include a dependence on planet phase and therefore is only valid around secondary ecilpse, when we see the "full" planet.

Planet thermal emission

We approximate the emergent intensity of the planet thermal emission by a blackbody curve at the planet's equilibrium temperature T_{p}. The latter is calculated by equating the rate at which energy carried by the host star radiation is absorbed to the rate at which the planet re-radiates this energy, thereby implicitly assuming

that stellar irradiation is the only relevant source of energy in the planet atmosphere. The temperature of the planet's day side is given by:

$$T_{\rm p} = T_* \sqrt{\frac{R_*}{a}} \sqrt[4]{\frac{1-A_{\rm B}}{4f}} \tag{3}$$

were R_* denotes the stellar radius, T_* the stellar effective temperature, a the distance between star and planet, $A_{\rm B}$ is the planetary Bond albedo, and f is the fraction of the planetary surface over which we assume the absorbed energy to be re-radiated, controlling the efficiency of day- to night-side heat re-distribution ($0.5 < f \leq 1$, where $f = 0.5$ corresponds to no heat-redistribution, i.e. all absorbed energy is re-radiated on the day side and the night side is cold, and $f = 1.0$ corresponds to complete heat-redistribution, i.e. day- and night side are equally warm). The thermal emission from the planet is given by:

$$F_{\rm p,t} = \frac{\pi R_{\rm p}^2}{d^2} B(T_{\rm p}, \lambda) \tag{4}$$

where $R_{\rm p}$ is the planet radius and $B(T_{\rm p}, \lambda)$ denotes the Planck function at the planet's temperature.

Observed eclipse depth

The total amount of light emerging from the planet is $F_{\rm p} = F_{\rm p,t} + F_{\rm p,r}$ and the measured eclipse depth $\xi(\lambda)$, which is in practice identical to the planet-to-star contrast ratio because $F_{\rm p} \ll F_*$, is given by:

$$\xi(\lambda) = \frac{F_{\rm p}}{F_* + F_{\rm p}} \approx \frac{F_{\rm p}}{F_*} = \frac{R_{\rm p}^2}{R_*^2} \, \frac{B(T_{\rm p}, \lambda)}{I(T_*, \lambda)} \; + \; x_{\rm r}(\lambda) \; A(\lambda) \; \frac{R_{\rm p}^2}{a^2} \tag{5}$$

where the first term represents the thermal emission and the second term the reflected light. Note that, alternatively, it is possible to provide the radiometric code with actual (model) planet spectra, to replace the simplified approach described above.

2.2.2 Day-night terminator absorption spectra in primary eclipse

The eclipse depth in primary eclipse is the fraction of stellar light blocked by the planet, which is approximately equal to the ratio of solid angles subtended by the planet and its host star, but shows minute wavelength-dependent variations if the high planeteary atmospheric layers contain spectroscopically active species. It is common to express the eclipse depth, i.e. the fraction of stellar light that is blocked by the planet as a function of wavelength, by the "effective radius" of the planet:

$$\xi(\lambda) = \left(\frac{R_{\rm p,eff}(\lambda)}{R_*} \right)^2 \equiv \left(\frac{R_{\rm p} + \Delta z(\lambda)}{R_*} \right)^2 \approx \frac{R_{\rm p}^2}{R_*^2} + \frac{2 R_{\rm p} \Delta z(\lambda)}{R_*^2} \tag{6}$$

Here, the last term represents the modulation of the transit depth due to spectral features, whose amplitude is expected to be approximately proportional to the pressure scale height H high in the exoplanet atmosphere. The latter is proportional to the temperature and inversely proportional to the planet's surface gravity g and the mean molecular weight μ in its atmosphere. We apply an approximate relation for the modulation amplitude of the main spectral bands:

$$\Delta z(\lambda) \approx 5H, \quad \text{with} \;\; H = \frac{k T_{\rm p}}{\mu g} \tag{7}$$

Such a relation has been demonstrated previously (e.g.[21] and we have independently confirmed that ≈ 5 is an appropriate average value for the constant of proportionality.[13] Note that, alternatively, it is possible to provide the radiometric code with actual (model) planet spectra, to replace the simplified approach described above.

2.2.3 Phase curves

The thermal emission spectra as a function of orbital phase, or for non-transiting systems, are currently not part of the radiometric code. The same is true for reflected light spectra as a function of orbital phase. The current model evaluates these quantities only around secondary eclipse.

3. THE RADIOMETRIC CODE: *EclipseSim*

The radiometric code *EclipseSim* models a standard, long-slit, dispersive spectrograph, using e.g. a prism or a single order of a grism per spectrometer channel. Fourier Transform Spectrographs are not considered. A cross-dispersed multiple-order concept is not explicitly included, but can be approximated by treating each order as an individual channel, with an appropriate blaze function.

The model presented here is purely radiometric, that is, it propagates the astrophysical signal through an instrument model, includes various sources of background radiation and detector noise, calculates the signal and noise budgets on the detector pixel level, and integrates these over each spectral resolution element and over time. Hence, it produces SNR estimates that reflect the fundamental performance limit, i.e. the SNR that is in principle reachable given the finite number of source photons that can be detected during an obseration, and the fundamental noise sources. Instrumental or astrophysical *systematic* effects, that may prevent reaching the fundamental SNR limit, are not taken into account. While our performance model does have built-in functionality to model instrumental systematic effects, this is beyond the scope of the current description and not part of the public release of *EclipseSim*. The fundamental effects that are included are:

- shot noise from the target
- zodiacal background
- thermal background from the telescope and instrument interior
- detectror dark current (DC) and readout noise (RON).

The radiometric model is coded in IDL and has a modular design in which all information is stored in a sigle structure that is passed on from one module to the next.

3.1 The astrophysics module

The purpose of the astrophysics module is to provide the radiometric calculation with appropriate input spectra and other relevant quantities. Stellar and planetary spectra are calculated as described in sections 2.1 and 2.2. At the longer wavelengths the zodiacal light may not be negligible compared to the stellar signal and we include it as a background emission component as described in appendix B.

Furthermore the astrophysics module calculates the orbital period and the duration of the eclipse timing parameters T_{14} (the time between the beginning in ingress and the end of egress, when the planet is partially in front of or behind the star) and T_{23} (the time between the end of ingress and the beginning of egress, when the planet is completely in front of or behind the star):

$$T_{14} = \frac{2a \sin^{-1}\left(\frac{R_* + R_\mathrm{p}}{a}\right)}{\sqrt{GM_*/a}} \qquad \text{and} \qquad T_{23} = \frac{2a \sin^{-1}\left(\frac{R_* - R_\mathrm{p}}{a}\right)}{\sqrt{GM_*/a}} \tag{8}$$

where G is the universal gravitational constant and M_* denotes the stellar mass.

3.2 The optics module

The optics module treats the propagation of the astrophysical signals to the detector in a parameterized way. The total system transmission can be given as a simple scalar fraction (with $0 \leq \text{transmission} \leq 1$) for each channel, but can also be any wavelength dependent function within each channel.

Subsequently the spectrum is imaged onto the detector, which requires defining the PSF shape in the spatial and spectral directions, as well as the number of detector elements with which a resolution element is sampled in each direction. The PSF in the spatial direction is assumed to be the diffraction limited beam, but it can optionally be widened by convolving it with a beam of constant width (to simulate, e.g., a small de-focus[§] in a simplified way). In the spectral direction the dispersion curve must be defined, for which there are three choices:

[§]Making the beam wider than the diffraction limit has negligible influence on the radiometry (except for faint sources at long wavelengths where the zodiacal background dominates over the star light) but may be beneficial for the photometric stability and reduce sensitivity to e.g. pointing jitter.

(1) a constant spectral resolution (i.e. $R = \lambda/\Delta\lambda$ is constant throughout a channel); (2) a constant dispersion (i.e. $\Delta\lambda$ is constant throughout a channel, so the spectral resolution R increases linearly with wavelength. The use of a grism or grating as a dispersive element will yield such a curve); (3) read a dispersion function of arbitrary shape from file, which can be used to model e.g. the non-linear dispersion of a prism.

3.3 The detector module

In the detector module all photon fluxes impinging on the detector pixels are converted into electron generation rates by multiplication with the QE, thus going from [γ/s/pix] to [e-/s/pix]. To get the total number of electrons released in each pixel per second the electron generation rates from all contributors are added:

$$e^-_{\rm tot} = e^-_{\rm s} + e^-_{\rm zodi} + e^-_{\rm tel} + e^-_{\rm inst} + e^-_{\rm dc} \tag{9}$$

where the sub-scripts s, zodi, tel, inst, and dc indicate the contributions from the star, the zodical background, the dispersed telescope thermal emission, the un-dispersed instrument interior thermal emission, and the dark current, respectively.

3.3.1 Detector duty cycle

The detector duty cycle is calculated such that the total number of electrons gathered in any pixel between two destructive readouts does not exceed a specified fraction of the full well capacity, 2/3 by default. To be compliant with a minimum cadence (temporal resolution), the time between two destructive readouts cannot exceed a specified value, 30s by default. This causes the detector wells to be filled to only a fraction of the maximum allowed value for faint sources. For bright sources, the time between destructive readouts can be substantially shorter than 30s. We assume a sampling up the ramp scheme in which there are a number of non-destructive readouts between each destructive readout, and a short reset time after each destructive readout.

3.3.2 Signal budget on the pixel level

A small correction is then applied to all electron generation rates to account for the duty cycle being smaller than 1. Typically the duty cycles are very close to one and this has no significant effect. The readout noise (RON) is assumed to be the total noise per destructive readout. The RON is converted to an effective RON per second (i.e. for a 30s cycle the effective RON per second would be smaller than the RON value per destructive readout by a factor $\sqrt{30}$). The SNR per pixel and per second elapsed time is then calculated in the following way:

$$SNR_1 = \frac{e^-_{\rm s,1}}{\sqrt{e^-_{\rm s,1} + e^-_{\rm zodi,1} + e^-_{\rm tel,1} + e^-_{\rm inst,1} + e^-_{\rm dc,1} + (e^-_{\rm ron,1})^2}} \tag{10}$$

where all electron generation rates are effective rates per second, corrected for the duty cycle, as indicated by the ",1" subscripts.

3.4 The SNR module

The total SNR that can be obtained per pixel on a spectrum during a given time t is obtained by multiplying SNR_1 with the square root of t. The SNR per resolution element is obtained by multiplying by the square root of the number of pixels by which a single resolution element is sampled (spatial $\times$ spectral PSF size). The time available to build up signal during an eclipse is assumed to be $T_{\rm eclipse} = (T_{14} + T_{23})/2$.

We then need to take into account that we are not measuring merely the "in-eclipse" spectrum, but instead wish to measure the "in- minus out-of-eclipse" difference, where we refer to the out-of-eclipse measurement as the "baseline". The SNR on the difference spectrum approaches that of the in-eclipse measurement in the limit $T_{\rm baseline} \to \infty$, i.e. $T_{\rm baseline} \gg T_{\rm eclipse}$. In practice, the eclipse duration will be a non-negligible fraction of the total observed time sequence, and the achieved SNR on the difference spectrum can be obtained from that of the in-eclipse spectrum by division by a factor $\sqrt{1 + 1/x}$, where x denotes the length of the baseline measurement in units of the elcipse duration.

Lastly, for challenging science cases, we may build up signal by integrating over multiple eclipse measurements. The SNR is then assumed to scale with the square root of the number of eclipses that are averaged. This

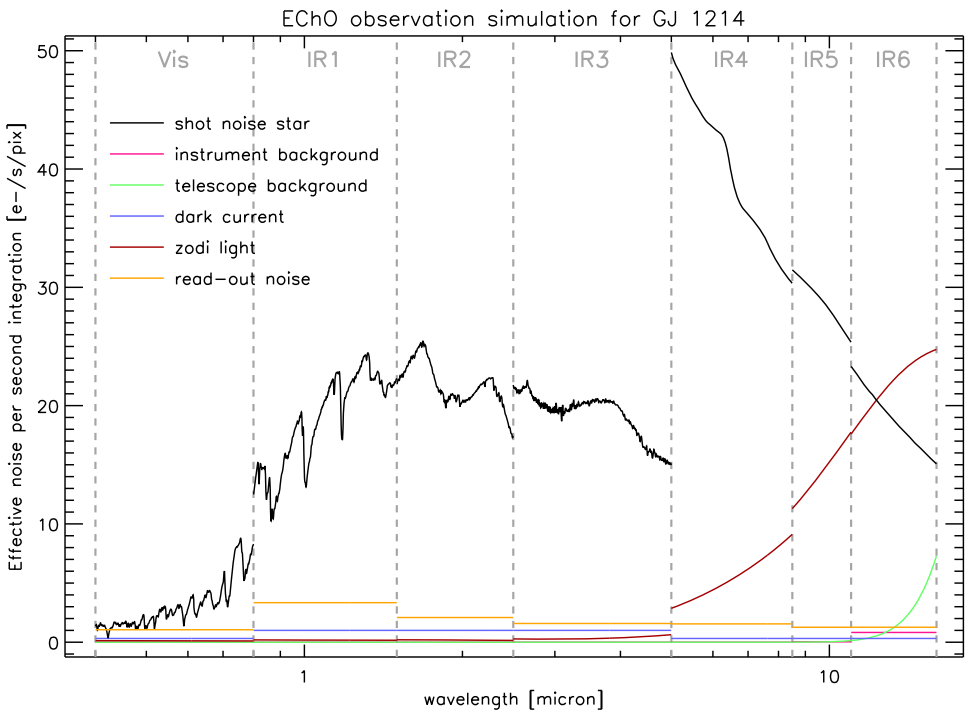

Figure 2. An illustration of the relative importance of the various noise contributions for a simulated observation of the GJ 1214 system with EChO as described by the parameters listed in table 1. Note that the instrumental parameters are not final. A color version of this figure is available online.

implicitly assumes that any temporal variations in the planet spectrum are small compared to the finally reached flux uncertainties, and, more importantly, that averaging over independent measurements does not introduce any systematic errors on that same level. The final signal to noise on the in-out eclipse difference spectrum then becomes:

$$SNR = SNR_1 \sqrt{\frac{T_{\rm eclipse}\ n_{\rm spat}\ n_{\rm spec}\ N_{\rm ecl}}{1+1/x}}\ , \qquad \text{with} \quad x \equiv \frac{T_{\rm baseline}}{T_{\rm eclipse}} \tag{11}$$

where $n_{\rm spat}$ and $n_{\rm spec}$ denote the number of detector pixels that sample a spatial and spectral resolution element, respectively, and $N_{\rm ecl}$ is the number of eclipses over which we average.

Note that it has also implicitly been assumed that the various additive backgrounds (including DC) are perfectly stable and are automatically canceled in the difference spectrum. If real time monitoring of the backgrounds is needed, i.e. the backgrounds will be sampled by other pixels than those measuring the stellar signal, this will introduce extra noise. If the variations are slow compared to the detector duty cycle, then we may average the background measurement over multiple frames, and the corresponding noise penalty will be reduced. Here, we have assumed that any such noise penalty is negligible compared to the fundamental performance limit.

3.4.1 Using the spectral dimension to increase SNR?

In this work we are calculating the SNR achievable on in-out eclipse difference spectra, treating each spectral resolution element independently. As a consequence, the SNR on the difference spectrum is lower than the SNR of the in-eclipse spectrum by a factor $\sqrt{1+1/x}$, which describes the noise arizing from the determination of the baseline flux level, i.e. the "normalization" of the light curve.

However, one may consider that the individual spectral resolution elements in the measurement of the stellar spectrum are not independent. This is most easily seen for the case of relatively early type stars at thermal infrared wavelengths, where the spectrum is close to the blackbody shape, i.e. smooth, without strong spectral

structure. In this case, we can in principle determine the flux level of the stellar spectrum in individual spectral resolution elements of our instrument to a much better precision than the actual measurement in that particular wavelength bin. We may use our knowledge of the spectral shape, and simultaneously fit data at many wavelengths, theoretically beating down the noise by a factor of $\sqrt{N_c}$, where N_c denotes the number of spectral resolution elements in the spectrum. The factor $\sqrt{1+1/x}$ in the denominator of equation 11 is then replaced by a different expression, which is different for the primary and secondary eclipse but in both cases yields a higher SNR, as we will detail below.

From a purely radiometric perspective this concept is a valid way to improve the theoretical SNR limit for the temporal difference spectrum. We stress, however, that this concept requires *two fundamental assumptions* to be made, for which it remains to be proven whether they can be fulfilled:

1. We know (or can model) the *spectral shape* of the stellar spectrum, at the resolution of the spectrograph, to a precision that is better than the ultimate contrast we wish to achieve on the temporal difference spectrum.
2. We can calibrate the relative spectral response of the instrument between different resolution elements to an accuracy that is better than the ultimate contrast we aim to achieve on the temporal difference spectrum.

A note on assumption (1): it is plausible that this can be achieved for relatively early type host stars until ∼early-K at mid-infrared wavelengths, but remains to be shown for the near-infrared range and for late type stars (beyond ∼mid-K also in the 6−15 μm range. A note on assumption (2): this aspect involves an implicit change in the philosophy of the transit method compared to the classical idea: we no longer record a relative signal over time using the same hardware (pixels and their readout electronics) that has to be *stable* over a certain time to a certain level, but instead we need in addition to calibrate physically different hardware (pixels) against each other to the same very high precision. This puts a qualitatively different, and more stringent, requirement on the instrument.

If one adopts the abovementioned assumptions, the $\sqrt{N_c}$ improvement on the determination of the stellar flux level leads the factor $\sqrt{\frac{1}{1+1/x}}$ in equation 11 to be replaced by a different expression. In the case of secondary eclipse observations we measure the star-only signal during the eclipse whereas the planet photons are recorded during the baseline measurement. The above-mentioned factor is in this case replaced by $\sqrt{\frac{N_c}{1+N_c/x}}$, allowing to reach an improved SNR by performing a longer baseline measurement. In the limit of $N_c \gg x$ this factor reduces to $\approx\sqrt{x}$, illustrating the theoretical gain in SNR with the square root of the duration of the baseline measurement. In primary eclipse observations we gather the planet signal during the eclipse whereas we see the full stellar flux (with a small contribution from the planetary night side) during the baseline measurement, to which the $\sqrt{N_c}$ advantage applies in this case (where the planet's night side emission is implicitly assumed to be negligible). The factor $\sqrt{\frac{1}{1+1/x}}$ in quation 11 is then replaced by a factor $\sqrt{\frac{xN_c}{1+xN_c}}$, which in the limit of $xN_c \gg 1$ reduces to $\approx$1.

Given that fulfilling the above-mentioned two fundamental assumptions is questionable, we adopt the classical approach and use the general formula that includes the factor $\sqrt{\frac{1}{1+1/x}}$, but makes no assumptions on our ability to know the stellar spectral shape and relative response of the system in different resolution elements to extreme precision. Instead, we typically assume a baseline length that is at least twice the eclipse duration ($x \gtrsim 2$) to beat down the noise introduced during the baseline measurement. The optimum value of x depends on the overheads of an observation relative to the eclipse duration, various practical (scheduling) constraints, and the (subjective) importance of the science case. In practice, clearly, using correlations in wavelength will be an essential part of data processing to correct for systematic effects that may otherwise prevent reaching the fundamental photon noise limit.

3.5 Output

Upon running a simulation the code returns an IDL structure containing a number of quantities, the most important of which are:

- the host star spectrum and the planetary absorption or emission spectrum

Table 1. Parameters used to model the ESA reference design for EChO

		channel names						
quantity	units	Vis	IR1	IR2	IR3	IR4	IR5	IR6
pixel size	[μm/pix]	15	18	18	18	25	25	25
pixel size	[arcsec/pix]	0.30	0.54	0.67	1.03	1.28	1.59	1.44
qantum efficiency		0.70	0.70	0.70	0.70	0.70	0.70	0.70
full well capacity	[e^-/pix]	200000	65000	65000	65000	200000	200000	200000
dark durrent	[e^-/s/pix]	0.1	1.0	1.0	1.0	0.1	0.1	0.1
readout noise	[e^-/pix]	10	30	18	15	12	12	12
transmission		0.191	0.284	0.278	0.378	0.418	0.418	0.326
spectral resolution		300	300	300	300	30	30	30
instrument temperature	[K]	140	45	45	45	35	35	30
slit width	[arcsec]	2.1	2.6	3.3	5.2	7.7	9.5	13.2

- signals from star, planet, and various backgrounds on the detector (pixel) level
- the $SNR(\lambda)$ curve on the stellar in-out eclipse difference spectrum and on the extracted planet spectrum at three spectral resolutions: the (high) resolution of the input model, the instrumental resolution, and (optionally) re-binned to a lower resolution. The SNR on a given quantity always refers to a single spectral resolution element.

In addition, some diagnostic plots are produced. In figure 2 we show, as an example, the relative contributions of the various signal components to the total noise budget for a simulated observation of the GJ 1214 system. These are simply the square root of the number of electrons generated per pixel and per second by each component contributing to the signal. At wavelengths where the stellar signal is much larger than all the other components the curve labeled "shot noise star" is approximately equal to the SNR on the stellar signal reached *per second* of integration time on the detector pixel level. Since a spectral resolution element is sampled by a number of pixels $n_{\rm pix}$, which is typically $\gtrsim 5$, the SNR per second per resolution element is a factor $\sqrt{n_{\rm pix}}$ larger. At $K = 8.8$ mag and with a spectral type of M4.5, GJ 1214 is within the foreseen brightness range of EChO targets, but is rather on the faint end, particularly so at optical wavelengths.

4. EXAMPLE APPLICATIONS

Here we show a few practical applications of our performance model, meant to demonstrate the capabilities of EChO for a few key science cases. Naturally, this is by no means exhaustive. In all cases, we use the parameters of the current ESA reference design (early 2012), which are listed in table 1, as input for the performance model calculations. We note, though, that this design is not final and more mature concepts with somewhat improved performance are being developed. When supplied with an appropriate input file containing the key system parameters and, if required for e.g. prism spectrographs, dispersion curves, our code can model any other facility.

4.1 Hot Jupiters

Hot Jupiters were among the first exoplanets to be discovered[22] and because they are less difficult to find than their smaller or cooler counterparts, they have strongly dominated the population of known exoplanets in early years. With the ever increasing sensitivity of radial velocity and transit surveys, this dominance no longer prevails. Now that the era of exoplanet characterization has started, history repeats and the early results have been mostly on hot Jupiter type planets as they yield the largest signals[¶]. However, only ≈1% of F-, G-, and K-type stars harbour a hot Jupiter companion,[23] hence these objects remain somewhat of a special class and are not the most representative for the exoplanet population as a whole. Nonetheless, hot Jupiter planets will

[¶]This statement refers to the transit-photometry and -spectroscopy work of recent years. Direct imaging work has focused instead on planets with large orbital radii (but also here, focus lies on young, and therefore still warm, objects).

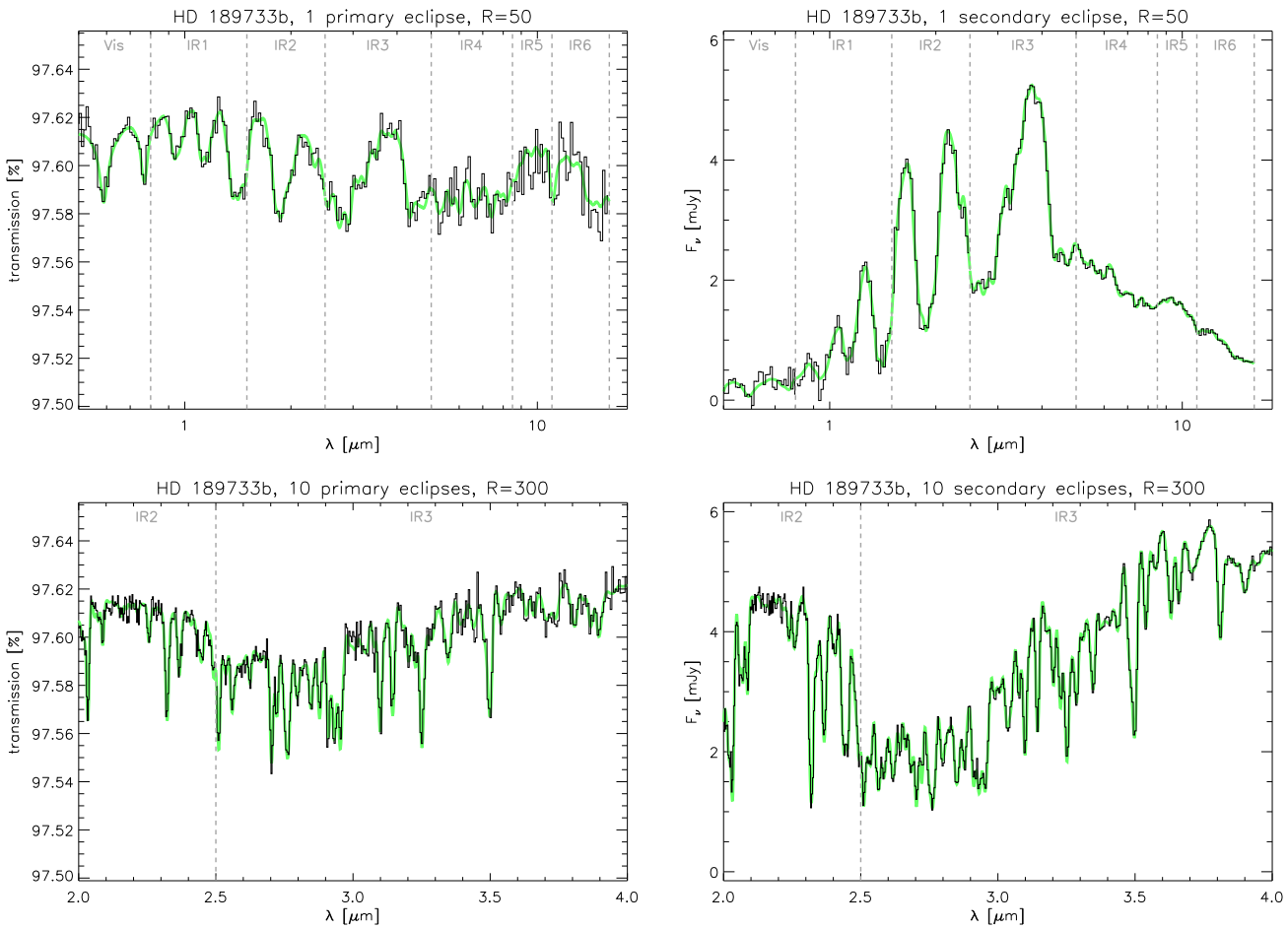

Figure 3. Simulated observations of HD 189733.[2] Top panels: primary and secondary eclipse observations re-binned to low resolution ($R = 50$), for a single eclipse measurement. Lower panels: zoom-in at $R = 300$ on the detailed spectral structure in the near-infared, 10 eclipses averaged. Model spectra are shown in green, simulated data are over-plotted in black. ESA reference design parameters (table 1) are used in the performance modeling. A color version of this figure is available online.

be a prime focus of any transit spectroscopy mission because their strong signals allow us to study them in most detail. While the dominant physical processes are not necessarily the same in various classes of planets of different temperatures, the laws of physics are universal and much of what we learn by studying these objects is relevant for the physics of smaller and cooler objects. While hot Jupiter planets are comparatively rare, their small orbital radii lead to high transit probabilities, making them strongly over-represented in samples of transiting planets.

In figure 3 we show simulated EChO observations of one of the best studied hot Jupiters, HD 189733 b, based on models that were fitted to broad-band photometric and low-resolution spectroscopic data obtained with Spitzer and HST.[2] In the top panel we show simulations of a single primary and secondary eclipse observation at a spectral resolution of $R = 50$, in which all the main ro-vibrational bands are detected at very high significance. This allows their relative strengths, and thereby the relative abundances of the main spectroscopically active species, to be accurately determined in a single eclipse observation. From the secondary eclipse observation we can also constrain the vertical temperature profile in the atmosphere and determine the optical albedo. In the lower panels we show a zoom-in on the near infared range, in which fine substructure within the individual ro-vibrational bands is detected with superb SNR at a resolution of $R = 300$ after averaging over several, in this

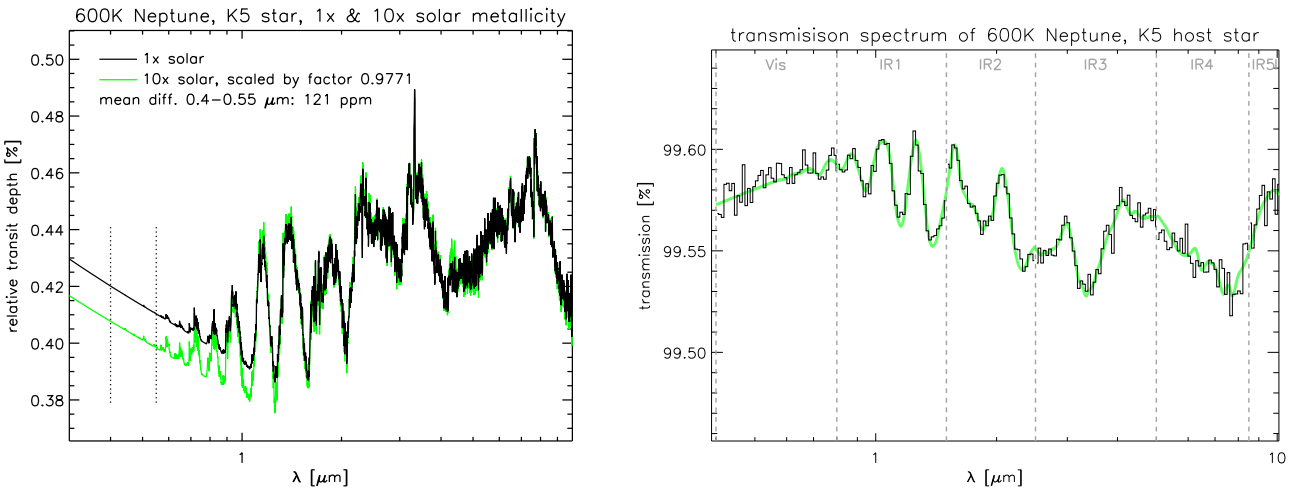

Figure 4. Primary transit absroption spectra of 600 K warm Neptunes. *Left*: relative transit depths of a planet with an equilibrium compositon atmosphere of solar metallicity (black) and one that is enriched in heavy elements (10× solar metallicity, green). The NIR transmission spectra are essentially identical, but the level of the optical Rayleigh scattering curve relative to the NIR range allows to distinguish both cases.[13] *Right*: simulated observations of a 600K warm Neptune with solar composition (ESA reference design parameters, see table 1, mid-K type host star at a distance of 50 pc ($K \approx 8.3$ mag), averaged over 10 eclipses). Note that the transmission (right plot) is 1 minus the relative transit depth (left plot). A color version of this figure is available online.

case 10, eclipses. These spectra rival those of early day, in-situ solar system exploration.

4.2 Neptunes & super-Earths

Neptune-type exoplanets differ from their larger Jupiter-type relatives in the sence that they are smaller and less massive, and H+He contribute much less to their total masses, though their atmospheres are likely to be still H+He dominated. A yet smaller class of planets, with a radius of $\lesssim 2$,$R_\oplus$ and masses in the $\approx 2-10\,M_\oplus$ range, have been dubbed "super-Earths", though it was realized that many of these objects may still have a thick H+He envelope and might more appropriately be referred to as "mini-Neptunes".

Here we use the term "super-Earth" for planets that consist largely of heavy elements, mostly refractory material (rock) and water (-ice), and the term (mini-) Neptune for objects in which H+He make up a substantial fraction of their their bulk mass. In terms of atmospheric characterization both cases are in principle very similar, except for a potential difference in mean molecular mass[‖].

EChO provides important advantages with respect to competing facilities such as Hubble, JWST, and the proposed JPL mission FINESSE, by offering large simultaneous wavelength coverage ($0.4-11\,\mu$m, with an optional extension to $16\,\mu$m, pending programmatic feasibility). For a sub-set of EChO targets we can:

1. provide a unique constraint of the mixing ratios of the atmospheric gases is possible by measuring (1) the transit depths in at least one absorption feature for each absorbing gas, and (2) the slope and strength of the molecular Rayleigh scattering signature at short wavelengths.[13] See Figure 4 for example primary transit absorption spectra of a 600 K warm Neptune.
2. discriminate between a thick, cloud-free atmosphere and an atmosphere with a surface, where the surface is either the ground or an opaque cloud deck. For an atmosphere with a surface at low optical depth, we can quantitatively constrain the pressure at this surface. A unique constraint of the composition is also possible for an atmosphere with a surface.[13]

[‖] Planets with a high mean molecular mass μ are observationally much more challenging in primary eclipse observations, because the spectral feature amplitude scales inversely with μ (see equation 7). For secondary eclipse observations, μ does not directly affect observational feasibility.

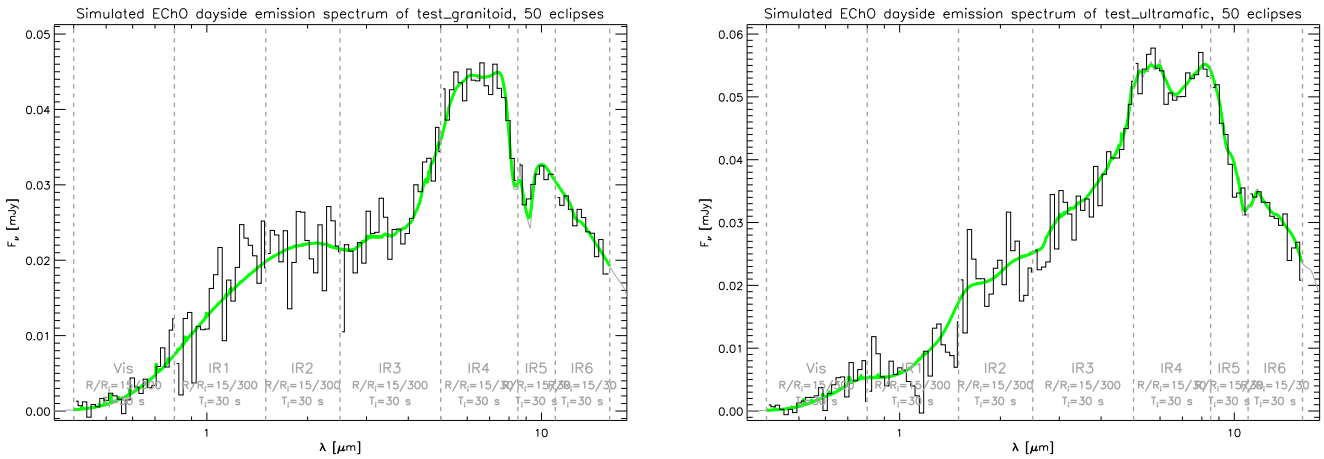

Figure 5. Simulated EChO spectra of hot, atmosphere-less rocky planets, orbiting a nearby M-type star (10 pc, $K \approx 8.8$ mag, spectral type M5). Both planets are $1.8\,R_\oplus$ in size and have an effective temperature of ≈850 K. ESA reference design parameters (table 1) assumed for performance model, and averaging over 50 eclipses. *Left*: a planet with a granitoid surface, indicative of slow cooling magma, pointing at plate tectonics. *Right*: a planet with an ultramafic surface, indicative of high-temperature, active volcanism.
A color version of this figure is available online.

3. discriminate between hydrogen-rich atmospheres and high mean molecular mass atmospheres, even in the presence of clouds.[13] An estimate of the mean molecular mass made independently of the other unknown atmospheric parameters is possible by measuring either the slope of the Rayleigh scattering signature, the shape of individual absorption features, or the relative transit depths in different features of the same molecular absorber.

4.2.1 Super-Earth surfaces

Both for (mini-) Neptunes and super-Earths the characterization of their atmospheres is the prime scientific objective. However, in the case of super-Earths with a very thin atmosphere, or no atmosphere at all, the exciting prospect of directly characterizing their rocky surfaces arizes. Here consider this possibility, and show that EChO has the capability to address this topic by measuring spectral features of the silicate surfaces of rocky, atmosphere-less exoplanets.

Silicate surfaces lead to unique features in the planetary thermal emission at mid-infrared wavelengths, most prominently the Si−O stretching mode at $7-13\,\mu$m.[24] We have simulated observations of rocky exoplanets having several types of silicate surfaces for nearby M dwarfs (figure 5). For hot super-Earths around nearby M-dwarfs, EChO will be able to detect the Si−O feature with moderate spectral resolution. Such a detection would directly confirm the exoplanet being predominantly rocky and break a common degeneracy between rocks and volatiles in the planetary mass-radius relationship.

Furthermore, the details of the Si−O feature, in particular the wavelength of the emissivity maximum at the short-wavelength edge of the feature, are indicative of the type of silicates (i.e. the Christiansen feature[24]). Granitoid material, for example, has an emission peak at $\approx 7.5\,\mu$m whereas emission from an ultramafic surface peaks at $\approx 8.5\,\mu$m. As is shown in figure 5, EChO could convincingly distinguish both cases. This may then be tied to the planets geological history. For example, ultramafic surfaces indicate primary crust from a magma ocean or high-temperature active volcanism, whereas granitold surfaces indicate reprocessing, heating and partial melting of the primary crust, a regime on Earth driven by plate tectonics.

4.2.2 Molecular features in temperate super-Earths around M-type stars

A major goal of exoplanet characterization efforts is to perform spectroscopy of temperate Earth-like planets, i.e. those with a rocky surface and a temperature allowing liquid water thereon, to detect molecules and ultimately bio-markers in their atmospheres.

Doing spectroscopy of a true Earth twin, i.e. a $1\,R_\oplus$ planet orbiting a Sun-like star, is beyond the scope of any conceivable transit spectroscopy mission, and requires large technology developments such as long baseline infrared interferometers consisting of multiple free-floating space-craft (TPF/Darwin) or highly sophisticated space coronagraphs. It was realized, however, that "super-Earth" planets in the temperate zone around M-type main sequence stars may be within reach of transit spectroscopy missions. Due to the much lower stellar luminosity, the orbital radii at which the appropriate temperatures prevail are much smaller than for Sun-like stars, increasing both the transit propability and the number of transits that occur in a given time interval. Moreover, the low stellar brightness yields a much more favorable planet/star contrast ratio compared to host stars of earlier spectral type. Observations have shown that temperate super-Earth (hereafter "TSE") planets are very common around M-type main sequence stars.[25]

Molecules leave their imprint in both primary transit absorption spectra and secondary transit emission spectra. If the atmosphere is dominated by species with a relatively low mean molecular mass, primary transit observations may provide the best prospects of detecting molecules in these objects. The dayside emission spectrum is to first approximation independent of H and we here consider secondary eclipse observations for these objects. Clearly, detecting molecules in TSE atmospheres is by far the most challenging science case for a transit spectroscopy mission such as EChO. Here we investigate out to what distance we may detect the key molecules Water, Carbon dioxide, and Ozone in secondary eclipse observations, around TSE planets orbiting M-type stars as a function of host star spectral type, under the following assumptions:

1. the planets have the same emergent intensity as Earth, but are bigger ($1.8\,R_\oplus$) and correspondingly brighter.
2. we observe and average over 50% of all eclipses that occur over a 5-year mission lifetime.

We use our performance model to simulate EChO spectra (see figure 6, left panel), on which we can then do detection experiments for the main spectral bands of H_2O ($\approx$5$-$8 μm), O_3 (9.3$-$10.1 μm), and CO_2 ($\approx$13$-$16 μm). The model we use to fit the simulated data is based on the actual input spectrum $F(\lambda)$ (green curve in figure 6), which we decompose into a smooth continuum and an absorption component $A_{\mathrm{abs}(\lambda)}$ for the respective molecular band we are fitting, which is given by:

$$A_{\mathrm{abs}}(\lambda) = 1 - \frac{F(\lambda)}{\Omega_{\mathrm{planet}} B(287\,\mathrm{K}, \lambda)} \tag{12}$$

where Ω_{planet} denotes the solid angle subtended by the planet, which we keep fixed to the input value throughout the whole process, assuming that we will know it comparatively accurately from primary eclipse observations. The model spectrum is then given by:

$$F_{\mathrm{model}}(\lambda) = \Omega_{\mathrm{planet}} B(T_{\mathrm{fit}}, \lambda)(1 - s_{\mathrm{fit}} A_{\mathrm{abs}}(\lambda)) \tag{13}$$

and has two free parameters: the dimensionless normalized depth of the absorption feature s_{fit} and the temperature of the underlying blackbody T_{fit}, of which the input values are 1.0 and 287 K, respectively. We perform a simple χ^2 minimization to find the optimum values of s_{fit} and T_{fit}.

We repeat this experiment many times, each time supplying the simulated spectrum with a fresh set of normally distributed noise according to the SNR that was given by the performance model. The resulting distribution of fitted values for s_{fit} and T_{fit} closely follows a gaussian distribution. Comparing the width σ_{s} of the s_{fit} distribution to its mean value of 1.0 yields an estimate of the significance of the detection of the respective molecular band: $n_\sigma = 1/\sigma_{\mathrm{s}}$. Lastly, we iteratively vary the distance to the source until we reach $n_\sigma = 3$, i.e. we have a $3\,\sigma$ detection of the molecular band. This is illustrated in the right panel of figure 6.

The SNR that we can reach on the planet spectra depends on the host star spectral type, and increases towards later spectral types because:

- the planet/star brighness contrast increases strongly towards later spectral types (we keep the planet size and temperature fixed to $1.8\,R_\oplus$ and 287 K, respectively).
- the orbital period at which an equilibrium temperature of 287 K is reached decreases as we go to later spectral types, allowing to average over more eclipses. Even though the duration of individual eclipses decreases somewhat towards later spectral types, the total amount of time available to gather signal increases.

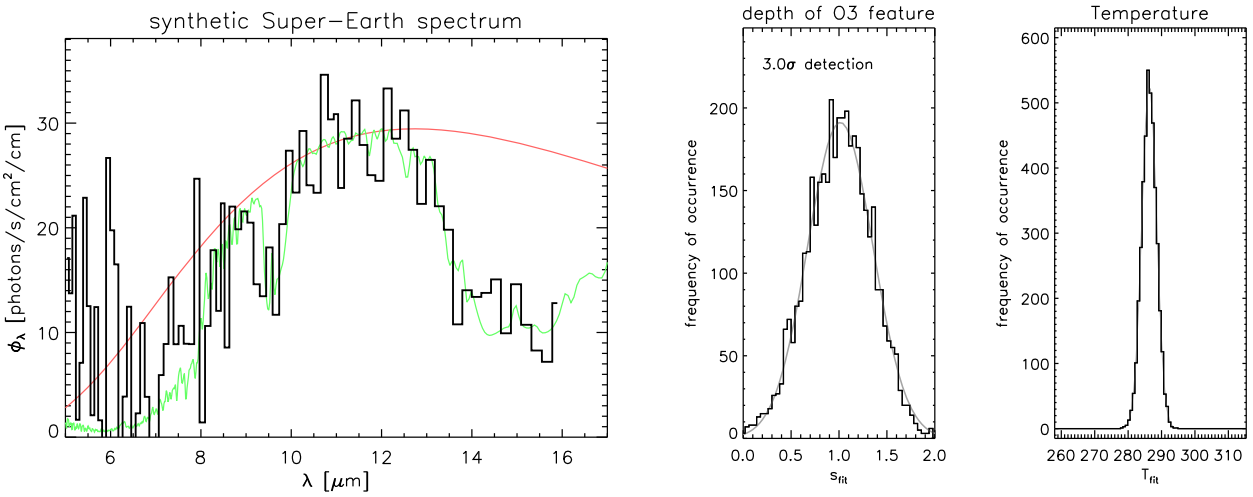

Figure 6. Feature detection in temperate Super-Earth spectra. *Left*: a simulated spectrum of a 1.8 $R_\oplus$ planet with an emergent intensity identical to Earth, orbiting an M5 star, as observed with a "current reference design" EChO (see table 1). The underlying imput spectrum is shown in green. The spectrum has been averaged over 122 eclipses and the distance to the source is 2.6 pc. *Right*: the distribution of fitted parameters of 2048 random renditions of this spectrum, with the same SNR. See section 4.2.2 for details. A color version of this figure is available online.

We perform the procedure described above for a range of host star spectral types, thereby determining out to what distance we can achieve $3\,\sigma$ detections of H_2O, O_3, and CO_2. The results are shown in figure 7, and a few aspects are worth noting:

1. CO_2 is the least difficult molecule to detect due to its high equivalent width and long wavelength (hence favorable planet/star contrast). H_2O is already much more difficult and O_3 is more difficult still.

2. the maximum distance $d_{\max}$ out to which a feature can be detected follows a slope as expected from the finite number of source photons noise limit for H_2O and O_3. For CO_2 the same is true up to a spectral type of ≈M4, after which the curve changes slope and the increase of $d_{\max}$ towards later spectral types becomes less steep. This is due to the zodiacal background, which becomes similarly bright as the host star at the limiting distance $d_{\max}$ around this spectral type, and dominates the signal at later spectral types. The change in slope thus corresponds to a transition from the source photon limited to the background limited regime.

Lastly, we show in the bottom right panel of figure 7 how the maximum distance out to which CO_2 can be detected with a transit spectroscopy mission, as a function of the facility's Figure of Merit (FoM), which is the product of the effective light gathering area, the total instrumental transmission Tr, and the detector quantum efficiency QE, and has units of [$m^2\,e^-$/photon]:

$$FoM = A_{\rm eff} Tr(\lambda) QE(\lambda) \tag{14}$$

The current EChO reference design has an FoM of aproximately 0.31 $m^2\,e^-$/photon (average value for channels IR4, IR5, IR6, covering 5-16 μm), but this value may increase somewhat as off-axis telescope designs offering larger apertures of up to ≈1.5m are considered, and IR instrument throughput may be further optimized.

From first principles we expect $d_{\max}$ to scale linearly with the telescope diameter D, and thus like the square root of the FoM (keeping the system transmission and detector QE constant), if detector duty cycle effects are ignored and the width of the PSF is assumed to scale inversely with the telescope size. This holds both in the source photon limited regime as well as in the background limited regime, though the slope q of linear relation $d_{\max} = qD$ is larger in the source photon limited regime than in the background limited regime. This behavior is indeed seen in the bottom right panel of figure 7.

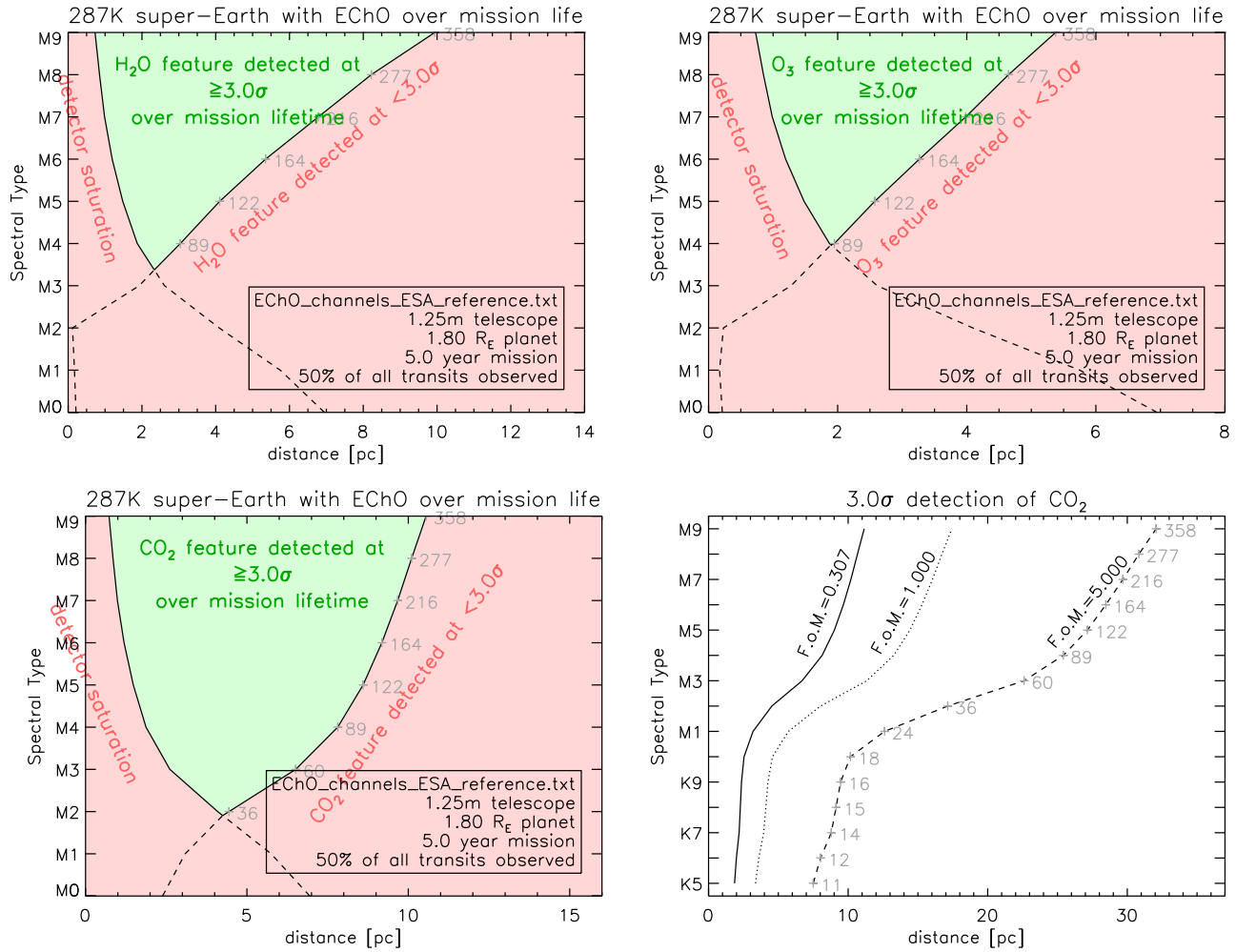

Figure 7. The maximum distance out to which the spectral bands of H_2O, O_3, and CO_2 can be detected in secondary eclipse observations of temperate Super-Earth planets of $1.8\,R_\oplus$, assuming their surface brightness is identical to that of the Earth. Parameters of the ESA reference model are assumed in the performance model (see table **??**). Grey numbers denote the number of eclipses over which the signal is averaged. A color version of this figure is available online.

Finally we note that in all of the above we have explored only the fundamental limits based on source- and background photon statistics. We have not considered any systematic effects, such as potential problems arising due to stellar activity and the associated variability.

5. SUMMARY

We have presented *EclipseSim*, a general tool to simulate exoplanet transit spectroscopy observations for both primary eclipse (day-night terminater absorption spectra) and secondary eclipse (day side emission spectra). The tool includes fundamental instrumental and astrophysical noise sources and as such provides an estimate of the maximum reachable performance of the modeled facility. All calculations are done in a spectrally resolved fashion and the tool provides visualization of the individual contributors to the noise budget as a function of wavelength. It also produces simulated data. *EclipseSim* is publicly available.

We have applied our tool to the *E*xoplanet *Ch*aracterization *O*bservatory (EChO), a proposed mission dedicated to exoplanet transit spectroscopy, that is currently in competition for the M3 launch slot in ESA's cosmic vision programme. We have shown a number of case studies on planets with sizes in the super-Earth to Jupiter

range, and temperatures ranging from the temperate to the ≈1500 K regime, demonstrating the power and versatility of EChO. A dedicated observatory, fine-tuned towards spectro-photometric stability, offers truly great perspectives and will hugely advance our knowledge of the physics of exoplanet atmospheres, and their full diversity.

APPENDIX A. STELLAR PARAMETERS

We use a mass-based grid containing 50 models with (initial) masses between 0.075 and 20 $M_\odot$, approximately logarithmically spaced. Assigning an effective temperature and radius to an object of a given initial stellar mass requires the use of stellar evolutionary tracks, and a choice of stellar age. We assume a star of a given spectral type to have an age corresponding to one-third of its nominal main sequence lifetime**, with a maximum of 10 Gyr.

For stars with masses between 0.6 and 5.2 $M_\odot$ we use the Yonsei-Yale tracks[27–30] complemented with the tracks by Baraffe[31] for stars below 0.6 $M_\odot$ and with those by Girardi et al.[32] for stars above 5.2 $M_\odot$. At this point, we have a set of 50 models with effective temperatures from ≈2,000 monotonically increasing to ≈34,000 K, each with the appropriate stellar radius, mass and age (the stellar luminosities and surface gravities are then implicitly fixed).

For each model calculate the emergent spectrum using PHOENIX models at effective temperatures below 10,000 K and ATLAS 9 models[33–35] at higher temperatures. We bin the models to a constant spectral resolution of $\lambda/\delta\lambda \approx 3{,}500$ over the whole included wavelength range (0.01 to 100 μm). We store the model spectra as specific intensities, which can be converted to observable fluxes by multiplying by the solid angle subtended by the star Ω_* as seen from Earth.

Effectively, we have a one-dimensional model grid and a model spectrum of any main sequence star in the covered temperature range can be obtained by linear interpolation in $\log T_{\rm eff}$. One can either specify $T_{\rm eff}$ or give a spectral type, which is then converted to effective temperature††. If no stellar radius R_* is specified this quantity will be adopted from the model grid, but it is also possible to explicitly set the radius‡‡. The absolute flux scale is finally set by specifying the distance to the star, thereby fixing Ω_*. Instead of giving the distance it is also possible to specify the K-band magnitude, which is then used to derive a photometric distance.

APPENDIX B. ZODIACAL LIGHT MODEL

The main astrophysical source of background radiation (or, rather, foreground radiation) relevant for EChO is the zodiacal light. We model it using the Kelsall et al. model[45] that is based on COBE/DIRBE measurements. The intensity of the zodiacal light is a strong function of viewing direction relative to the ecliptic and the Sun-vector. The pointing restrictions as currently baselined for EChO are that the spacecraft can rotate freely (360°) about the Sun vector, and approximately 36° away from the plane normal to the sun vector in both directions. Thus, on average, a target is observable ≈59% of the time, assuming a uniform sky distribution of sources.

We have calculated an average zodiacal light intensity over the viewing angles accessible by EChO as described above, where we have weighted the intensity of each viewing direction over ecliptic lattitude with the fraction of time a source at each lattitude is observable. The resulting average intensities in the COBE/DIRBE bands are shown in figure 8, together with a spline fit to these values (black curve). We use this spline fit to evaluate the intensity of the zodiacal light at arbitrary wavelengths. Also shown in figure 8 are the highest and lowest values of the zodiacal light intensity occurring within the pointing restrictions, corresponding to pointings near the ecliptic plane and the ecliptic poles, respectively. By default we use the mean intensity curve in all our radiometric calculations.

**We crudely approximate the main sequence lifetime of a star with $10 \times \left(\frac{M_*}{M_\odot}\right)^{-2.5}$ Gyr.[26]

††For spectral types from B2 to G9 we use the relation derived by,[36] between K0 and K9 we use that by,[37] and between M0 and M9 we approximate a large number of data points[38–44] with the linear relation $T_{\rm eff} = 3800 - 160\,x$, where x denotes the M-dwarf subtype.

‡‡We then ignore that this may introduce a slight mis-match between the actual $\log g$ and that used in the model spectrum. At the level of precision required for the current application, the inferred small potential differences in flux are irrelevant.

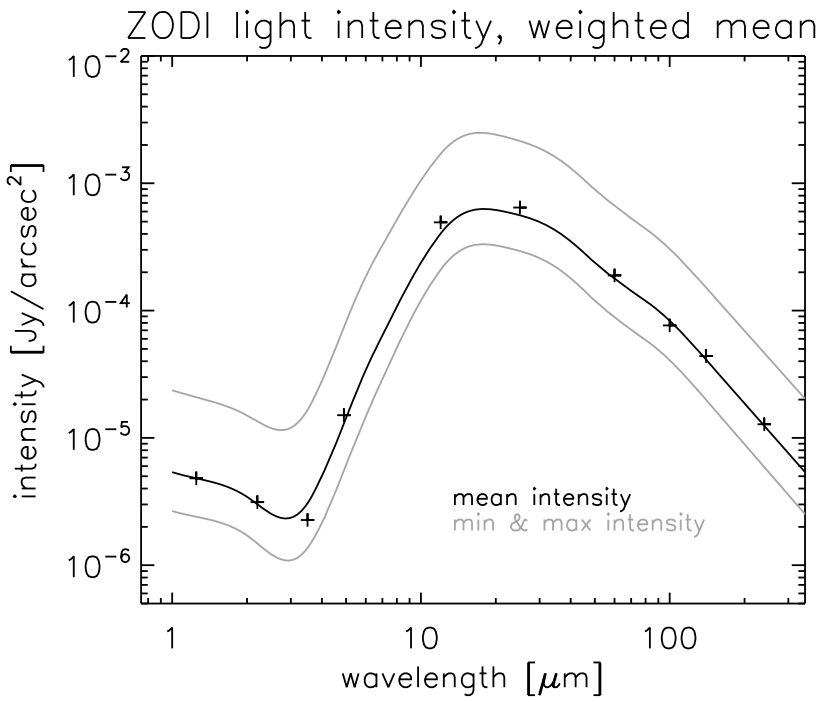

Figure 8. Mean zodiacal light intensity over the viewing directions accessible to EChO (black curve), as well as the minimum and maximum intensities. Based on COBE/DIRBE measurements[45]

ACKNOWLEDGMENTS

We gratefully acknowledge Kate Isaak, Marc Ollivier, and Ludovic Puig for a successful experiment in which our radiometric model was benchmarked with codes developed at ESA and in Paris.[20] We thank Marc Ollivier, Ingo Waldmann, Ignasi Ribas, and Giovanna Tinetti for an insightful discussion that led us to include section 3.4.1.

REFERENCES

[1] Seager, S. and Deming, D., "Exoplanet Atmospheres," *ARA&A* **48**, 631–672 (Sept. 2010).

[2] Madhusudhan, N. and Seager, S., "A Temperature and Abundance Retrieval Method for Exoplanet Atmospheres," *ApJ* **707**, 24–39 (Dec. 2009).

[3] Showman, A. P., Fortney, J. J., Lian, Y., Marley, M. S., Freedman, R. S., Knutson, H. A., and Charbonneau, D., "Atmospheric Circulation of Hot Jupiters: Coupled Radiative-Dynamical General Circulation Model Simulations of HD 189733b and HD 209458b," *ApJ* **699**, 564–584 (July 2009).

[4] Heng, K., Menou, K., and Phillipps, P. J., "Atmospheric circulation of tidally locked exoplanets: a suite of benchmark tests for dynamical solvers," *MNRAS* **413**, 2380–2402 (June 2011).

[5] Swain, M. R., Vasisht, G., Henning, T., Tinetti, G., and Beaulieu, J.-P., "THESIS: the terrestrial habitable-zone exoplanet spectroscopy infrared spacecraft," in [*Space Telescopes and Instrumentation 2010: Optical, Infrared, and Millimeter Wave. Edited by Oschmann, Jacobus M., Jr.; Clampin, Mark C.; MacEwen, Howard A. Proceedings of the SPIE, Volume 7731, pp. 773125-773125-7 (2010).*], **7731** (July 2010).

[6] Tinetti, G., Beaulieu, J. P., Henning, T., Meyer, M., Micela, G., Ribas, I., Stam, D., Swain, M., Krause, O., Ollivier, M., Pace, E., Swinyard, B., Aylward, A., van Boekel, R., Coradini, A., Encrenaz, T., Snellen, I., Zapatero-Osorio, M. R., Bouwman, J., Y-K. Cho, J., Coudé du Foresto, V., Guillot, T., Lopez-Morales, M., Mueller-Wodarg, I., Palle, E., Selsis, F., Sozzetti, A., Ade, P. A. R., Achilleos, N., Adriani, A., Agnor, C. B., Afonso, C., Allende Prieto, C., Bakos, G., Barber, R. J., Barlow, M., Bernath, P., Bezard, B., Bordé, P., Brown, L. R., Cassan, A., Cavarroc, C., Ciaravella, A., Cockell, C. O. U., Coustenis, A., Danielski, C., Decin,

L., De Kok, R., Demangeon, O., Deroo, P., Doel, P., Drossart, P., Fletcher, L. N., Focardi, M., Forget, F., Fossey, S., Fouqué, P., Frith, J., Galand, M., Gaulme, P., González Hernández, J. I., Grasset, O., Grassi, D., Grenfell, J. L., Griffin, M. J., Griffith, C. A., Grözinger, U., Guedel, M., Guio, P., Hainaut, O., Hargreaves, R., Hauschildt, P. H., Heng, K., Heyrovsky, D., Hueso, R., Irwin, P., Kaltenegger, L., Kervella, P., Kipping, D., Koskinen, T. T., Kovács, G., La Barbera, A., Lammer, H., Lellouch, E., Leto, G., Lopez Morales, M., Lopez Valverde, M. A., Lopez-Puertas, M., Lovis, C., Maggio, A., Maillard, J. P., Maldonado Prado, J., Marquette, J. B., Martin-Torres, F. J., Maxted, P., Miller, S., Molinari, S., Montes, D., Moro-Martin, A., Moses, J. I., Mousis, O., Nguyen Tuong, N., Nelson, R., Orton, G. S., Pantin, E., Pascale, E., Pezzuto, S., Pinfield, D., Poretti, E., Prinja, R., Prisinzano, L., Rees, J. M., Reiners, A., Samuel, B., Sanchez-Lavega, A., Sanz Forcada, J., Sasselov, D., Savini, G., Sicardy, B., Smith, A., Stixrude, L., Strazzulla, G., Tennyson, J., Tessenyi, M., Vasisht, G., Vinatier, S., Viti, S., Waldmann, I., White, G. J., Widemann, T., Wordsworth, R., Yelle, R., Yung, Y., and Yurchenko, S. N., "EChO - Exoplanet Characterisation Observatory," *eprint arXiv:1112.2728* (Dec. 2011).

[7] Charbonneau, D., Brown, T. M., Noyes, R. W., and Gilliland, R. L., "Detection of an Extrasolar Planet Atmosphere," *ApJ* **568**, 377–384 (Mar. 2002).

[8] Tinetti, G., Vidal-Madjar, A., Liang, M.-C., Beaulieu, J.-P., Yung, Y., Carey, S., Barber, R. J., Tennyson, J., Ribas, I., Allard, N., Ballester, G. E., Sing, D. K., and Selsis, F., "Water vapour in the atmosphere of a transiting extrasolar planet," *Nature* **448**, 169–171 (July 2007).

[9] Pont, F., Knutson, H., Gilliland, R. L., Moutou, C., and Charbonneau, D., "Detection of atmospheric haze on an extrasolar planet: the 0.55-1.05 μm transmission spectrum of HD 189733b with the HubbleSpaceTelescope," *MNRAS* **385**, 109–118 (Mar. 2008).

[10] Sing, D. K., Pont, F., Aigrain, S., Charbonneau, D., Désert, J.-M., Gibson, N., Gilliland, R., Hayek, W., Henry, G., Knutson, H., Lecavelier Des Etangs, A., Mazeh, T., and Shporer, A., "Hubble Space Telescope transmission spectroscopy of the exoplanet HD 189733b: high-altitude atmospheric haze in the optical and near-ultraviolet with STIS," *MNRAS* **416**, 1443–1455 (Sept. 2011).

[11] Gibson, N. P., Aigrain, S., Pont, F., Sing, D. K., Désert, J.-M., Evans, T. M., Henry, G., Husnoo, N., and Knutson, H., "Probing the haze in the atmosphere of HD 189733b with Hubble Space Telescope/WFC3 transmission spectroscopy," *MNRAS* **422**, 753–760 (May 2012).

[12] de Mooij, E. J. W., Brogi, M., de Kok, R. J., Koppenhoefer, J., Nefs, S. V., Snellen, I. A. G., Greiner, J., Hanse, J., Heinsbroek, R. C., Lee, C. H., and van der Werf, P. P., "Optical to near-infrared transit observations of super-Earth GJ 1214b: water-world or mini-Neptune?," *A&A* **538**, A46 (Feb. 2012).

[13] Benneke, B. and Seager, S., "Atmospheric Retrieval for Super-Earth Atmospheres: Uniquely Constraining the Atmospheric Composition with Transmission Spectroscopy," *ArXiv e-prints* (Mar. 2012).

[14] Öberg, K. I., Murray-Clay, R., and Bergin, E. A., "The Effects of Snowlines on C/O in Planetary Atmospheres," *ApJ* **743**, L16 (Dec. 2011).

[15] Madhusudhan, N., Mousis, O., Johnson, T. V., and Lunine, J. I., "Carbon-rich Giant Planets: Atmospheric Chemistry, Thermal Inversions, Spectra, and Formation Conditions," *ApJ* **743**, 191 (Dec. 2011).

[16] Heng, K., Hayek, W., Pont, F., and Sing, D. K., "On the effects of clouds and hazes in the atmospheres of hot Jupiters: semi-analytical temperature-pressure profiles," *MNRAS* **420**, 20–36 (Feb. 2012).

[17] Burrows, A., Hubeny, I., Budaj, J., Knutson, H. A., and Charbonneau, D., "Theoretical Spectral Models of the Planet HD 209458b with a Thermal Inversion and Water Emission Bands," *ApJ* **668**, L171–L174 (Oct. 2007).

[18] Cowan, N. B. and Agol, E., "The Statistics of Albedo and Heat Recirculation on Hot Exoplanets," *ApJ* **729**, 54 (Mar. 2011).

[19] Perna, R., Heng, K., and Pont, F., "The Effects of Irradiation on Hot Jovian Atmospheres: Heat Redistribution and Energy Dissipation," *ApJ* **751**, 59 (May 2012).

[20] Tessenyi, M., Ollivier, M., Tinetti, G., Beaulieu, J. P., Coudé du Foresto, V., Encrenaz, T., Micela, G., Swinyard, B., Ribas, I., Aylward, A., Tennyson, J., Swain, M. R., Sozzetti, A., Vasisht, G., and Deroo, P., "Characterizing the Atmospheres of Transiting Planets with a Dedicated Space Telescope," *ApJ* **746**, 45 (Feb. 2012).

[21] Miller-Ricci, E., Seager, S., and Sasselov, D., "The Atmospheric Signatures of Super-Earths: How to Distinguish Between Hydrogen-Rich and Hydrogen-Poor Atmospheres," *ApJ* **690**, 1056–1067 (Jan. 2009).

[22] Mayor, M. and Queloz, D., "A Jupiter-mass companion to a solar-type star," *Nature* **378**, 355–359 (Nov. 1995).

[23] Mayor, M., Marmier, M., Lovis, C., Udry, S., Ségransan, D., Pepe, F., Benz, W., Bertaux, J. ., Bouchy, F., Dumusque, X., Lo Curto, G., Mordasini, C., Queloz, D., and Santos, N. C., "The HARPS search for southern extra-solar planets XXXIV. Occurrence, mass distribution and orbital properties of super-Earths and Neptune-mass planets," *ArXiv e-prints* (Sept. 2011).

[24] Hu, R., Ehlmann, B. L., and Seager, S., "Theoretical Spectra of Terrestrial Exoplanet Surfaces," *ApJ* **752**, 7 (June 2012).

[25] Bonfils, X., Delfosse, X., Udry, S., Forveille, T., Mayor, M., Perrier, C., Bouchy, F., Gillon, M., Lovis, C., Pepe, F., Queloz, D., Santos, N. C., Ségransan, D., and Bertaux, J.-L., "The HARPS search for southern extra-solar planets XXXI. The M-dwarf sample," *ArXiv e-prints* (Nov. 2011).

[26] Hansen, C. J. and Kawaler, S. D., [*Stellar Interiors. Physical Principles, Structure, and Evolution.*] (1994).

[27] Yi, S., Demarque, P., Kim, Y.-C., Lee, Y.-W., Ree, C. H., Lejeune, T., and Barnes, S., "Toward Better Age Estimates for Stellar Populations: The Y^2 Isochrones for Solar Mixture," *ApJS* **136**, 417–437 (Oct. 2001).

[28] Kim, Y.-C., Demarque, P., Yi, S. K., and Alexander, D. R., "The Y^2 Isochrones for α-Element Enhanced Mixtures," *ApJS* **143**, 499–511 (Dec. 2002).

[29] Yi, S. K., Kim, Y.-C., and Demarque, P., "The Y^2 Stellar Evolutionary Tracks," *ApJS* **144**, 259–261 (Feb. 2003).

[30] Demarque, P., Woo, J.-H., Kim, Y.-C., and Yi, S. K., "Y^2 Isochrones with an Improved Core Overshoot Treatment," *ApJS* **155**, 667–674 (Dec. 2004).

[31] Baraffe, I., Chabrier, G., Allard, F., and Hauschildt, P. H., "Evolutionary models for solar metallicity low-mass stars: mass-magnitude relationships and color-magnitude diagrams," *A&A* **337**, 403–412 (Sept. 1998).

[32] Girardi, L., Bertelli, G., Bressan, A., Chiosi, C., Groenewegen, M. A. T., Marigo, P., Salasnich, B., and Weiss, A., "Theoretical isochrones in several photometric systems. I. Johnson-Cousins-Glass, HST/WFPC2, HST/NICMOS, Washington, and ESO Imaging Survey filter sets," *A&A* **391**, 195–212 (Aug. 2002).

[33] Kurucz, R. L., "Model atmospheres for G, F, A, B, and O stars," *ApJS* **40**, 1–340 (May 1979).

[34] Kurucz, R. L., "Model Atmospheres for Population Synthesis," in [*IAU Symp. 149: The Stellar Populations of Galaxies*], 225–+ (1992).

[35] Kurucz, R., "Solar abundance model atmospheres for 0,1,2,4,8 km/s.," *Solar abundance model atmospheres for 0,1,2,4,8 km/s. Kurucz CD-ROM No. 19. Cambridge, Mass.: Smithsonian Astrophysical Observatory, 1994.* **19** (1994).

[36] Gray, R. O. and Corbally, C. J., "The calibration of MK spectral classes using spectral synthesis. 1: The effective temperature calibration of dwarf stars," *AJ* **107**, 742–746 (Feb. 1994).

[37] Schmidt-Kaler, T., [*The Physical Parameters of the Stars*], vol. VI of *in: Landolt-Börnstein*, Springer, Berlin, Heidelberg, New York (1982).

[38] Johnson, H. L., "Infrared Photometry of M-Dwarf Stars.," *ApJ* **141**, 170–+ (Jan. 1965).

[39] Bessell, M. S., "The late-M dwarfs," *AJ* **101**, 662–676 (Feb. 1991).

[40] Gizis, J. E., "M-Subdwarfs: Spectroscopic Classification and the Metallicity Scale," *AJ* **113**, 806–822 (Feb. 1997).

[41] Martín, E. L., Delfosse, X., Basri, G., Goldman, B., Forveille, T., and Zapatero Osorio, M. R., "Spectroscopic Classification of Late-M and L Field Dwarfs," *AJ* **118**, 2466–2482 (Nov. 1999).

[42] Leggett, S. K., Allard, F., Dahn, C., Hauschildt, P. H., Kerr, T. H., and Rayner, J., "Spectral Energy Distributions for Disk and Halo M Dwarfs," *ApJ* **535**, 965–974 (June 2000).

[43] Dahn, C. C., Harris, H. C., Vrba, F. J., Guetter, H. H., Canzian, B., Henden, A. A., Levine, S. E., Luginbuhl, C. B., Monet, A. K. B., Monet, D. G., Pier, J. R., Stone, R. C., Walker, R. L., Burgasser, A. J., Gizis, J. E., Kirkpatrick, J. D., Liebert, J., and Reid, I. N., "Astrometry and Photometry for Cool Dwarfs and Brown Dwarfs," *AJ* **124**, 1170–1189 (Aug. 2002).

[44] Reyle, C., Rajpurohit, A. S., Schultheis, M., and Allard, F., "The Effective temperature scale of M dwarfs from spectral synthesis," *ArXiv e-prints* (Feb. 2011).

[45] Kelsall, T., Weiland, J. L., Franz, B. A., Reach, W. T., Arendt, R. G., Dwek, E., Freudenreich, H. T., Hauser, M. G., Moseley, S. H., Odegard, N. P., Silverberg, R. F., and Wright, E. L., "The COBE Diffuse Infrared Background Experiment Search for the Cosmic Infrared Background. II. Model of the Interplanetary Dust Cloud," *ApJ* **508**, 44–73 (Nov. 1998).